# Quantifying the non-Abelian property of Andreev bound states in inhomogeneous Majorana nanowires

Yu Zhang

*School of Physics, MOE Key Laboratory for Non-equilibrium Synthesis and Modulation of Condensed Matter,*
*Xi'an Jiaotong University, Xi'an 710049, China*

Yijia Wu

*Interdisciplinary Center for Theoretical Physics and Information Sciences, Fudan University, Shanghai 200433, China*
*and Hefei National Laboratory, Hefei 230088, China*

Jie Liu*

*School of Physics, MOE Key Laboratory for Non-equilibrium Synthesis and Modulation of Condensed Matter,*
*Xi'an Jiaotong University, Xi'an 710049, China*
*and Hefei National Laboratory, Hefei 230088, China*

X. C. Xie

*Interdisciplinary Center for Theoretical Physics and Information Sciences, Fudan University, Shanghai 200433, China;*
*International Center for Quantum Materials, School of Physics, Peking University, Beijing 100871, China;*
*and Hefei National Laboratory, Hefei 230088, China*

Non-Abelian braiding is a key property of Majorana zero modes (MZMs) that can be utilized for topological quantum computation. However, the presence of trivial Andreev bound states (ABSs) in topological superconductors can hinder the non-Abelian braiding of MZMs. We systematically investigate the braiding properties of ABSs induced by various inhomogeneous potentials in nanowires and quantify the main obstacles to non-Abelian braiding. We find that if a trivial ABS is present at zero energy with a tiny energy fluctuation, the non-Abelian braiding property can be sustained for a larger braiding time cost since the undesired dynamic phase is suppressed. Under certain conditions, the non-Abelian braiding of ABSs can even surpass that of MZMs in realistic systems, suggesting that nearly zero energy ABSs with a tiny energy fluctuation might also be suitable for quantum computation.

## I. INTRODUCTION

The semiconductor-superconductor nanowire has been deemed one of the most promising platforms for pursuing Majorana zero modes (MZMs) [1–8]. After the first semiconductor-superconductor nanowire system was fabricated in 2012 [9], such systems have been fabricated in a number of experiments [10–20]. However, none of them can convincingly demonstrate the existence of MZMs in such systems. The central issue is that trivial Andreev bound states (ABSs) can mimic the signal of MZMs [21–39], making them difficult to distinguish using standard conductance measurement methods. These ABSs are induced by inhomogeneous potential or disorder, which is difficult to eliminate with state-of-the-art nanotechnology. Unlike the MZMs, which are nonlocally distributed at both ends of the nanowire, these states are partially separated in space and exhibit less topological protection. In principle, nonlocal conductance

measurements could be a powerful method to distinguish these two types of states [40–53]. However, other possibilities are still hard to rule out [54–56].

The most fundamental way to distinguish MZMs from the ABSs is based on its non-Abelian statistics [57–63]. When two MZMs are spatially exchanged, they obey an unusual rule, $\gamma_i \rightarrow \gamma_j$ and $\gamma_j \rightarrow -\gamma_i$. This braiding rotates the degenerate ground state formed by MZMs and constitutes the basic logic gate of the quantum computation [64]. Thus, investigating the braiding properties of MZMs in the presence of ABSs not only can distinguish the MZMs from the ABSs in principle but also is a necessary step towards the topological quantum computation. Although several groups have suggested that ABSs may also be utilized for non-Abelian braiding [24,29,65], direct investigations of their non-Abelian braiding properties are still lacking. Previously, we revealed that ABSs with finite energy can introduce an additional dynamic phase that disrupts non-Abelian braiding. The key factors that are detrimental to this process remain an open question. Furthermore, ABSs can be induced by various effects, such as inhomogeneities in the chemical potential, superconducting strength,

---

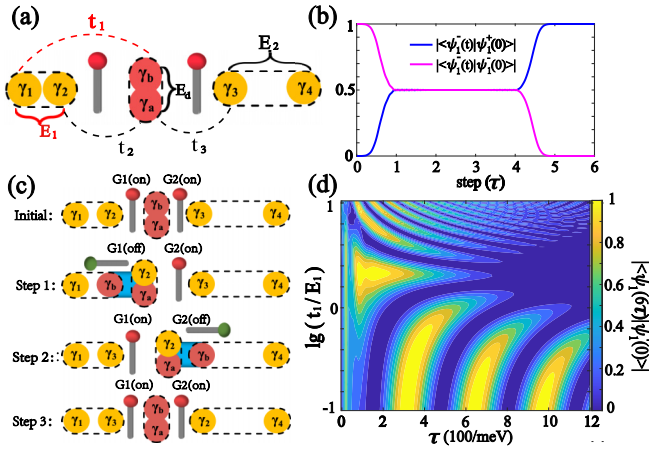*Contact author: jieliuphy@xjtu.edu.cn

FIG. 1. (a) Schematic diagram of a minimal effective model for braiding, where MZMs can be moved and swapped with the assistance of a QD by adjusting the coupling strengths. (b) Time evolution of the wave function $|\psi_1^-(t)\rangle$ for a perfect MZM with $E_1 = 0$ and $t_1 = 0$. The wave function evolves into $|\psi_1^+(0)\rangle$ after two successive swaps of $\gamma_2$ and $\gamma_3$. Here, we set $t_2 = t_3 = 0.3$ meV and $E_d = 0.3$ meV. (c) Braiding operation steps for non-Abelian braiding. $\gamma_2$ and $\gamma_3$ can be exchanged by sequentially turning the gates $G_1$ and $G_2$ on and off. (d) The braiding results as a function of $\tau$ with the influence of $t_1$ and $E_1$. Here, we fix $E_1 = 0.01$ meV. The other parameters are the same as in (b).

and disorder [30,31,36,66,67]. Knowing how to quantify the difference in these ABSs in different mechanism is certainly necessary. Quantifying the non-Abelian braiding properties of ABSs in different mechanism not only provides a perspective for distinguishing MZMs from ABSs from the viewpoint of non-Abelian braiding but also sheds light on how to recover non-Abelian braiding in the presence of ABSs.

In this paper, we try to quantify the braiding properties of these ABSs in various situations. We primarily focus on nearly zero energy ABSs, which display quantized zero-bias peaks (ZBPs) during conductance measurements, making them difficult to distinguish from MZMs through conductance measurements. We find that these nearly zero energy ABSs can be treated as two weakly coupled MZMs in a short nanowire. Although they are close to zero energy, they partially overlap in space. As shown in Fig. 1(a), the partially overlapping MZM $\gamma_1$ can hybridize with the exchanged MZM $\gamma_2$, resulting in a weak coupling $E_1$. Furthermore, $\gamma_1$ can also induce additional coupling $t_1$ with the auxiliary quantum dot (which is composed of $\gamma_a$ and $\gamma_b$). Both $E_1$ and $t_1$ can induce a dynamic phase and ruin the non-Abelian braiding. Interestingly, $t_1$ is closely related to $E_1$ in these nearly zero energy ABSs during the braiding. They oscillate with almost the same order of oscillation period. That is to say, if $E_1$ remains stable around zero energy with tiny energy fluctuations, $t_1$ will also be very small in that region. Then the braiding properties of these ABSs are similar to those of true MZMs. This suggests that nearly zero energy ABSs could potentially be used for quantum computation. In fact, we find that under certain conditions, these ABSs might even outperform true MZMs during braiding. Furthermore, since $E_1$ can be roughly measured through conductance, conductance measurements

may be a useful tool for detecting states that may be suitable for non-Abelian braiding.

The rest of this article is organized as follows. In Sec. II, we introduce the Hamiltonian of a low-energy effective braiding model and show the results of braiding under the influence of $E_1$ and $t_1$. In Sec. III, we introduce the tight-binding model of a realistic semiconductor-superconductor nanowire. Then we investigate the braiding property of ABSs in various situations. In Sec. III A we investigate the braiding property of MZMs under the influence of the length effect. In Sec. III B we show the braiding property of ABSs induced by an inhomogeneous chemical potential. In Sec. III C we investigate the braiding property of ABSs caused by a quantum-dot-like structure, and in Sec. III D we show the influence of disorder. In Sec. III E we show that the non-Abelian braiding may be modified by an inhomogeneous potential. Finally, in Sec. IV we provide a conclusion on the braiding properties of ABSs.

## II. EFFECTIVE MODEL FOR BRAIDING ABSs

To investigate the braiding properties in the presence of ABSs, we follow the proposal suggested in Ref. [60], in which the MZMs are braided with the assistance of a quantum dot (QD). In this setup, an additional QD is incorporated into the Josephson junction. Since MZMs are self-Hermitian particles with half the degree of an ordinary fermion, they couple only with the corresponding half degree of the fermionic state in the QD. By adjusting the coupling strengths between the MZMs and the QD using gate voltages, MZMs can effectively transfer in and out of the QD, allowing $\gamma_2$ and $\gamma_3$ to be exchanged via the QD. For the braiding of ABSs, the left side of the system is replaced by an inhomogeneous or disordered nanowire, with an ABS localized at its end, as shown in Fig. 1(a). The right side, however, remains an ideal semiconductor-superconductor nanowire with a pair of MZMs nonlocally distributed at the two ends. These MZMs, $\gamma_3$ and $\gamma_4$, are assumed to be well separated, with the coupling energy $E_2$ between them being zero. Our simulations in the concrete model suggest that these nearly zero energy ABSs can be deemed a pair of finite-overlap MZMs, $\gamma_1$ and $\gamma_2$, with the coupling energy $E_1$. What is more, $\gamma_2$ and $\gamma_3$ will sequentially couple to the auxiliary QD by turning off the corresponding gate, as revealed in Fig. 1(c). $\gamma_1$ will also couple to the QD when we turn off the gate $G_1$. Thus, the whole effective Hamiltonian describing this setup is given by

$$H_E(t) = 2E_d d^\dagger d + iE_1\gamma_1\gamma_2 + i[t_2(t)d + t_2(t)^*d^\dagger]\gamma_2$$
$$+ [t_1(t)^*d^\dagger - t_1(t)d]\gamma_1 + [t_3(t)d - t_3(t)^*d^\dagger]\gamma_3. \quad (1)$$

Here, $d$ is the annihilation operator for the fermionic state in the QD, and $E_d$ is the on-site energy of this QD state. In addition, the coupling strengths between the QD and $\gamma_1$, $\gamma_2$, and $\gamma_3$ are $t_1(t) = |t_1(t)|e^{i\phi_1/2}$, $t_2(t) = |t_2(t)|e^{i\phi_1/2}$, and $t_3(t) = |t_3(t)|e^{i\phi_2/2}$, respectively. Here, the phases $\phi_1$ and $\phi_2$ are the superconducting phases of the two nanowires, respectively. Following the proposal in Ref. [60], we set $\phi_1 - \phi_2 = \pi$ to facilitate the braiding. What is more, we can express the QD state in terms of the two Majorana operators $\gamma_a$ and $\gamma_b$ as $d = \frac{1}{2}e^{-i\frac{\phi_1}{2}}(\gamma_a + i\gamma_b)$. Therefore, the above Hamiltonian can

be further expressed by the Majorana operators as

$$H_{\text{EM}}(t) = iE_d\gamma_a\gamma_b + iE_1\gamma_1\gamma_2 + i|t_2(t)|\gamma_a\gamma_2 - i|t_1(t)|\gamma_b\gamma_1$$
$$- i|t_3(t)|\gamma_a\gamma_3. \tag{2}$$

If we set $E_1$ and $t_1(t)$ to zero, then this Hamiltonian can return to the previous Y-junction minimal model for braiding MZMs. The operation is consistent with previous manipulations [60,68] with only minor modifications. It can be summarized in three steps, with the time cost for each step denoted as $\tau$. Initially, the junctions are disconnected from each other; that is, $t_2(0) = t_3(0) = 0$, and $E_d$ is set to a nonzero initial value $E_0$. In step 1, we turn off the gate $G_1$; then $t_2$ increases as $t_2(t) = \frac{1-\cos(\frac{t}{\tau}\pi)}{2}t_c$, and simultaneously, $E_d$ is changed to zero as $E_d(t) = \frac{1+\cos(\frac{t}{\tau}\pi)}{2}E_0$ through gate voltage (not shown). In step 2, $|t_3(t)|$ increases from zero to $t_c$ as $t_3(t) = \frac{1-\cos(\frac{t}{\tau}\pi)}{2}t_c$ by turning off the gate $G_2$; simultaneously, we turn on the gate $G_1$, and then $t_2$ decreases as $t_2(t) = \frac{1+\cos(\frac{t}{\tau}\pi)}{2}t_c$. Finally, in step 3, we turn on the gate $G_2$, $|t_3|$ decreases to zero as $t_3(t) = \frac{1+\cos(\frac{t}{\tau}\pi)}{2}t_c$, and $E_d$ returns back to the initial value as $E_d(t) = \frac{1-\cos(\frac{t}{\tau}\pi)}{2}E_0$. Then all the parameters return to their initial forms, while $\gamma_2$ is exchanged with $\gamma_3$, with the exchange rule $\gamma_2 \to \gamma_3$ and $\gamma_3 \to -\gamma_2$. For two pairs of MZMs composed of nonlocal fermionic states, the effective Hamiltonian in each separate wire before braiding is in the form of $H_{j,\text{eff}} = iE_j\gamma_{2j-1}\gamma_{2j}(j = 1, 2)$. Hence, the eigenstates are in the wave functions of $|\psi_j^{\pm}(0)\rangle = \frac{1}{\sqrt{2}}(u_{2j-1} \pm iu_{2j})$, $u_{2j-1}$ and $u_{2j}$ are the normalized wave function of $\gamma_{2j-1}$ and $\gamma_{2j}$. If $\gamma_2$ and $\gamma_3$ are swapped twice in succession, then the wave function will evolve to $|\psi_1^{\pm}(6\tau)\rangle = \frac{1}{\sqrt{2}}(u_1 \mp iu_2) = |\psi_1^{\mp}(0)\rangle$ and $|\psi_2^{\pm}(6\tau)\rangle = \frac{1}{\sqrt{2}}(-u_3 \pm iu_4) = -|\psi_2^{\mp}(0)\rangle$. The simulation results confirm that $|\langle\psi_1^{-}(6\tau)|\psi_1^{+}(0)\rangle| = 1$ and $|\langle\psi_1^{-}(6\tau)|\psi_1^{-}(0)\rangle| = 0$ after $\gamma_2$ and $\gamma_3$ are adiabatically swapped twice in succession, as shown in Fig. 1(b). This evolution result demonstrates the non-Abelian braiding properties of MZMs.

In contrast, for the ABS state, these results no longer hold true since $E_1$ and $t_1$ are not strictly zero. Following the results of Ref. [69], the wave function will evolve as $|\psi_j^{\pm}(t)\rangle =$

$U(t)|\psi_j^{\pm}(0)\rangle$, with $U(t) = \hat{T}\exp[-i\int_0^t dt'H_{\text{EM}}(t')]$. The hybridizations between $\gamma_1$ and $\gamma_2$ and between $\gamma_1$ and $\gamma_b$ introduce the dynamic phase into the braiding operation. Consequently, the entire braiding operation is described not solely by the braiding operator $B^2(\gamma_2, \gamma_3)$, but rather by the unitary operator $U(6\tau) = \hat{T}\exp\{-i\int_0^{6\tau}dt[E_{1,\text{eff}}(t)\gamma_1\gamma_2 + t_{1,\text{eff}}\gamma_3\gamma_1 + \Omega\gamma_2\gamma_3]\}$, which incorporates both geometric and dynamic contributions. Here, $\Omega$ is the geometric phase, which is independent of the time cost $\tau$. It is exactly $\pi/2$ if we exchange $\gamma_2$ and $\gamma_3$ twice. In an even- or odd-parity qubit space, we can define the qubit operator [63,70,71] as $\sigma_x = -i\gamma_2\gamma_3$, $\sigma_y = -i\gamma_3\gamma_1$, and $\sigma_z = -i\gamma_1\gamma_2$. Then $\exp(-i\int dt\Omega\gamma_2\gamma_3) = \exp(\frac{\pi}{2}\sigma_x)$ is exactly a NOT gate which rotates $|\psi_j^{\pm}\rangle$ to $|\psi_j^{\mp}\rangle$. Meanwhile, $E_{1,\text{eff}}$ and $t_{1,\text{eff}}$ are the effective dynamic phase induced by the additional coupling terms $E_1$ and $t_1$, respectively. They will accumulate during the braiding and become dominant when the braiding time cost $\tau$ is large. Figure 1(d) numerically calculates the weight of $|\psi_1^{-}(6\tau)\rangle$ on $|\psi_1^{+}(0)\rangle$ versus the time cost $\tau$ and $t_1$; we fix $E_1$ as 0.001meV during the braiding. Since $t_1$ is manipulated by the gate $G_1$, it varies as $t_1(t) = \frac{1-\cos(\frac{t}{\tau}\pi)}{2}t_1$ when we turn off the gate, and $t_1(t) = \frac{1+\cos(\frac{t}{\tau}\pi)}{2}t_1$ when we turn on the gate $G_1$. Clearly, $|\langle\psi_1^{-}(6\tau)|\psi_1^{+}(0)\rangle|$ will approach 1 despite the influence of the nonadiabatic effect if $\tau$ approaches zero since the $\Omega$ term dominates in this situation. As $\tau$ increases, the dynamic phase becomes dominant. If $t_1$ is small, the $E_1$ term dominates and rotates the qubit space along the $z$ axis, causing $|\langle\psi_1^{-}(6\tau)|\psi_1^{+}(0)\rangle|$ to oscillate over time. As $t_1$ increases, the oscillation period also increases, but the amplitude quickly dampens to zero due to the noncommuting nature of $E_{1,\text{eff}}\sigma_z$ and $t_{1,\text{eff}}\sigma_y$. In contrast, when $t_1 \gg E_1$, the $t_1$ term is dominant and rotates the qubit space along the $y$ axis, leading to rapid oscillations of the weight due to the large $t_1$. In summary, the weight oscillates with time when only $E_1$ or $t_1$ is present, but it dampens due to their noncommuting nature. Finally, we want to emphasize that the dynamical behavior induced by $E_1$ and $t_1$ may vary for different paths. However, when the path is fixed, the dynamical behavior is primarily related to the ratio of $E_1$ and $t_1$. Thus, we can quantify $E_1$ and $t_1$ by analyzing the oscillatory behavior of the wave function.

TABLE I. Parameters for potential and superconducting pairing amplitude in different physical mechanism.

| Physical mechanism | $\mu$ (meV) | $V(x)$ (meV) | $\Delta$ (meV) | $\alpha$ (meV nm) | $L$ (μm) |
|---|---|---|---|---|---|
| Uniform nanowire | 0 | 0 | 0.25 | 40 | 1.5 |
| Steplike IP[a] | 1.2 | $V(x) = \begin{cases} 0 & \text{if } x < 2.3 \\ 1.2 & \text{if } x \geqslant 2.3 \end{cases}$ | 0.25 | 40 | 2.5 |
| Smooth IP[a] | 1.5 | $V(x) = \begin{cases} 0 & \text{if } x < 1.875 \\ 1.5\sin(\frac{(x-1.875)\pi}{1.25}) & \text{if } x \geqslant 1.875 \end{cases}$ | 0.25 | 40 | 2.5 |
| Steplike QD | 0.4 | $V(x) = \begin{cases} 0 & \text{if } x < 2.3 \\ 0.4 & \text{if } x \geqslant 2.3 \end{cases}$ | $\Delta(x) = \begin{cases} 0.25 & \text{if } x < 2.3 \\ 0 & \text{if } x \geqslant 2.3 \end{cases}$ | 40 | 2.5 |
| Smooth QD | 1 | $V(x) = \begin{cases} 0 & \text{if } x < 1.75 \\ 1\sin(\frac{(x-1.75)\pi}{1.5}) & \text{if } x \geqslant 1.75 \end{cases}$ | $\Delta(x) = \begin{cases} 0.25 & \text{if } x < 1.75 \\ 0 & \text{if } x \geqslant 1.75 \end{cases}$ | 40 | 2.5 |
| Disorder | 1 | $V(x) \sim \mathcal{N}(0, 1^2)$ | 0.25 | 40 | 2.5 |

[a]IP: Inhomogeneous potential.
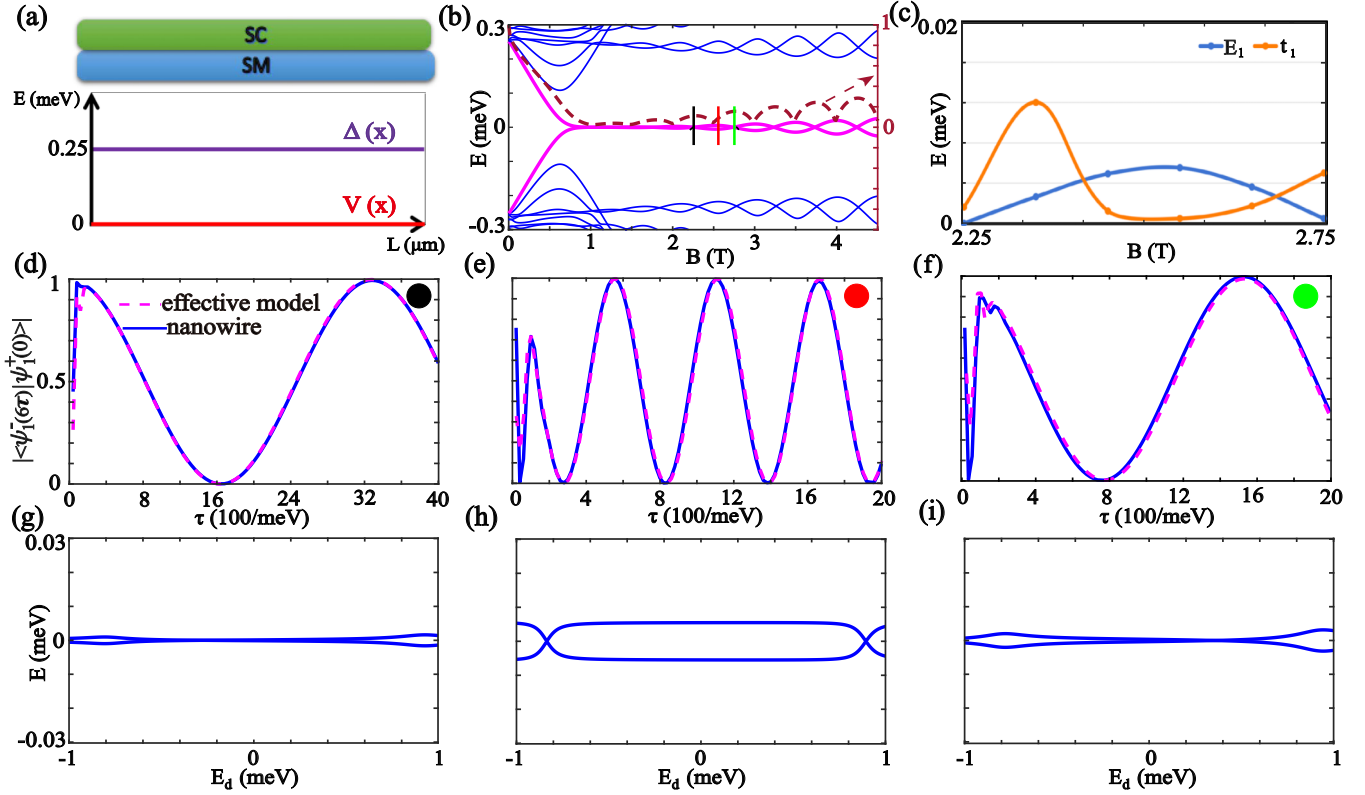
FIG. 2. Uniform nanowire with finite length. (a) The top panel shows a schematic plot of the uniform nanowire model. The bottom panel displays the distributions of $\Delta(x)$ and $V(x)$. The purple solid line represents the distribution of $\Delta(x)$ along the nanowire, while the red solid line corresponds to $V(x)$ along the nanowire, as described by the first row of Table I. (b) Energy spectrum of a finite-length nanowire. Majorana zero modes (MZMs) oscillate around zero energy due to the finite length of the nanowire. The dark red dashed line indicates the corresponding local estimator $\eta$,, suggesting that the MZMs are nonlocally distributed. (c) The value of $E_1$ and the corresponding effective $t_1$ retrieved by fitting the effective model. Here, we focus on the range from $B = 2.25$ T to $B = 2.75$ T. (d)–(f) Typical braiding results as a function of braiding time cost $\tau$. These results correspond to the values of $B$ marked by the vertical lines in different colors in the energy spectrum in (b) (indicated by the solid line). The dashed line presents the fitting result from the effective model. (g)–(i) Energy spectrum of the quantum-dot–nanowire model as a function of the on-site energy $E_d$ with different $B$, which also correspond to the values of $B$ marked by the vertical lines in different colors in the energy spectrum of (b). In (d) and (g), $B = 2.25$ T, $E_1 = 3.368 \times 10^{-5}$ meV, and the corresponding effective $t_1 = 2.00 \times 10^{-3}$ meV. In (e) and (h), $B = 2.55$ T, $E_1 = 5.500 \times 10^{-3}$ meV, and the corresponding effective $t_1 = 2.00 \times 10^{-4}$ meV. In (f) and (i), $B = 2.75$ T, $E_1 = 4.885 \times 10^{-4}$ meV, and the corresponding effective $t_1 = 5.10 \times 10^{-3}$ meV.

## III. NUMERICAL SIMULATION IN A REAL SEMICONDUCTOR-SUPERCONDUCTOR NANOWIRE

Since ABSs are caused by inhomogeneous potential or disorder in a semiconductor-superconductor nanowire, we need to introduce a realistic system to simulate the ABSs. The Hamiltonian for the whole system is given as follows:

$$H_T(t) = \sum_{i=1,2} H_{Si} + H_C(t) + H_D. \tag{3}$$

Here, $H_{S1(2)}$ is the tight-binding Hamiltonian of the semiconductor-superconductor nanowire which stays on the left (right) side of the QD; it is given by

$$H_{Si} = \sum_{\mathbf{x},\alpha} -t_0(\psi^\dagger_{i\mathbf{x}+\mathbf{a},\alpha} \psi_{i\mathbf{x},\alpha} + \text{H.c.}) - \mu \psi^\dagger_{i\mathbf{x},\alpha} \psi_{i\mathbf{x},\alpha}$$

$$+ \sum_{\mathbf{x},\alpha,\beta} -iU_R \psi^\dagger_{i\mathbf{x}+\mathbf{a},\alpha} \hat{z} \cdot (\vec{\sigma}_y)^{\alpha\beta} \psi_{i\mathbf{x},\beta}$$

$$+ \sum_{\mathbf{x},\alpha} \Delta(x)e^{i\phi} \psi^\dagger_{i\mathbf{x},\alpha} \psi^\dagger_{i\mathbf{x},-\alpha} + V(x)\psi^\dagger_{i\mathbf{x},\alpha} \psi_{i\mathbf{x},\alpha}$$

$$+ \sum_{\mathbf{x},\alpha,\beta} \psi^\dagger_{i\mathbf{x},\alpha} (g\mu_B B\vec{\sigma}_x)_{\alpha\beta} \psi_{i\mathbf{x},\beta} + \text{H.c.} \tag{4}$$

Here, the subscript $\mathbf{x}$ denotes the lattice site, $\mathbf{a}$ is the lattice constant, $\alpha$ and $\beta$ are the spin indices, $t_0 = h^2/(2m^*a^2)$ denotes the hopping amplitude, $\mu$ is the chemical potential of the nanowire, $U_R = \alpha/(2a)$ is the Rashba coupling strength, and $g\mu_B B$ is the Zeeman energy, with $g$ being the effective $g$ factor, $\mu_B$ being the Bohr magneton, and $B$ being the magnetic field. $\Delta(x)$ is the superconducting pairing amplitude of site $x$. Here, we keep $\Delta(x)$ a constant value $\Delta$ on the right side of the nanowire, and it may vary for different sites on the left side of the nanowire since it is an inhomogeneous nanowire. For the same reason, we introduce $V(x)$ to describe the inhomogeneous chemical potential or disorder of site $x$. It is zero on the right side of the nanowire but varies for different sites on the left side of the nanowire. In Table I, we give the parameters for
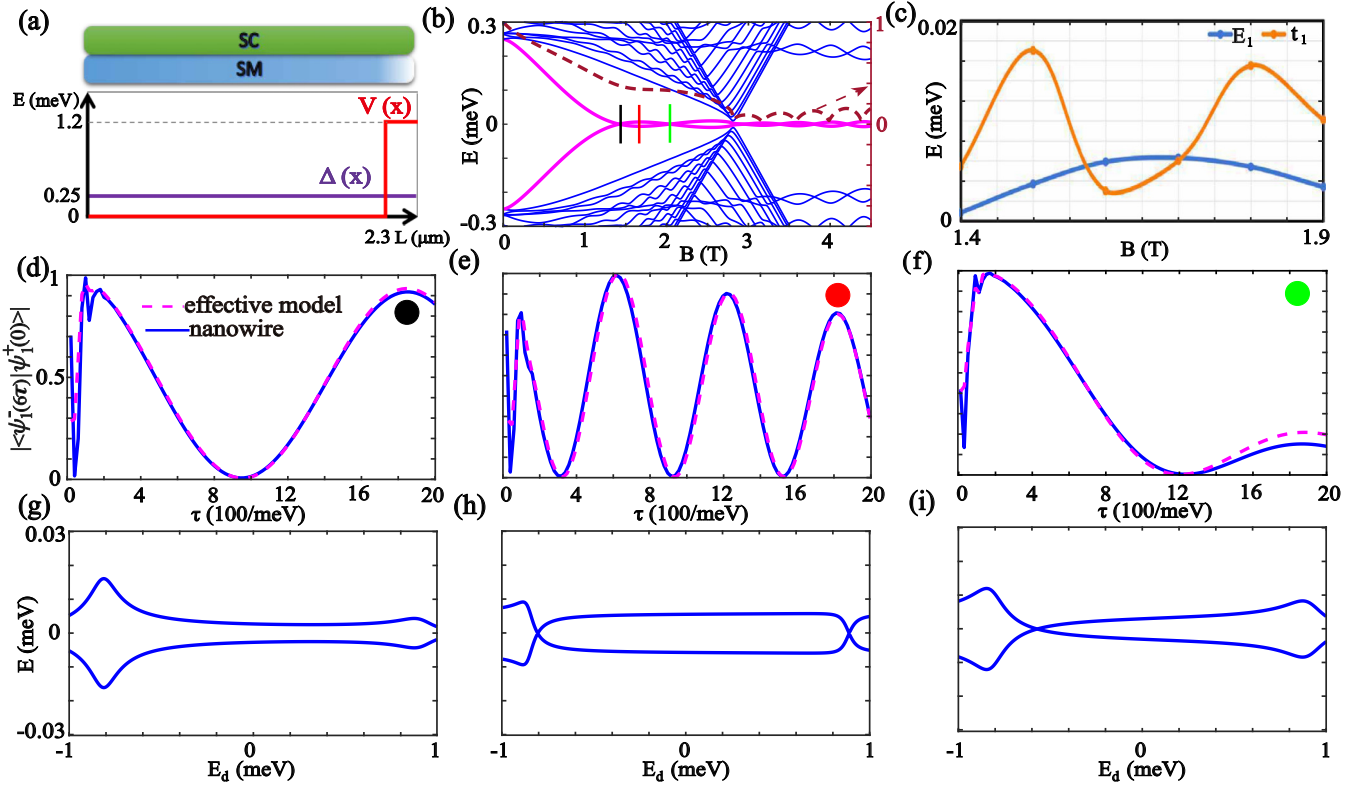
FIG. 3. Steplike inhomogeneous potential. (a) Schematic of the steplike inhomogeneous potential model, along with the corresponding distributions of $\Delta(x)$ and $V(x)$. (b) Energy spectrum of the steplike inhomogeneous potential model, with the corresponding local estimator $\eta$ indicated by the dark red dashed line. (c) The value of $E_1$ and the corresponding effective $t_1$, focusing on the range from $B = 1.4\,\mathrm{T}$ to $B = 1.9\,\mathrm{T}$. (d)–(f) Braiding results as a function of braiding time cost $\tau$ at different values of $B$, which are marked by the vertical lines in different colors in the energy spectrum in (b). The dashed line represents the fitting result from the effective model. (g)–(i) The corresponding energy spectrum of the quantum-dot–nanowire model as a function of $E_d$. In (d) and (g), $B = 1.4\,\mathrm{T}$, $E_1 = 8.289 \times 10^{-4}\,\mathrm{meV}$, and the corresponding effective $t_1 = 5.10 \times 10^{-3}\,\mathrm{meV}$. In (e) and (h), $B = 1.6\,\mathrm{T}$, $E_1 = 5.900 \times 10^{-3}\,\mathrm{meV}$, and the corresponding effective $t_1 = 2.00 \times 10^{-3}\,\mathrm{meV}$. In (f) and (i), $B = 1.9\,\mathrm{T}$, $E_1 = 3.400 \times 10^{-3}\,\mathrm{meV}$, and the corresponding effective $t_1 = 9.25 \times 10^{-3}\,\mathrm{meV}$. The other parameters are shown in the second row of Table I.

five typical types of inhomogeneous cases which can induce nearly zero energy ABSs. The other parameters are given as follows: The effective mass $m^* = 0.026m_e$, where $m_e$ is the electron rest mass, the Rashba spin-orbit coupling strength $\alpha = 30\,\mathrm{meV\,nm}$, $\Delta = 0.25\,\mathrm{meV}$, $g = 15$, and the lattice constant $a = 25\,\mathrm{nm}$.

$H_d$ is the Hamiltonian of the QD; we introduce a Zeeman term to break the degeneracy of the spin:

$$H_d = \sum_{\alpha} 2E_d d_\alpha^\dagger d_\alpha + \sum_{\alpha,\beta} d_\alpha^\dagger (V_x \vec{\sigma}_x)_{\alpha\beta} d_\beta. \tag{5}$$

$H_C(t)$ describes the coupling between the ends of two nanowires and the QD:

$$H_C(t) = \sum_{i=1,2;\alpha} C_i(t) \psi_{i,x_{end},\alpha}^\dagger d_\alpha + \mathrm{H.c.} \tag{6}$$

Here, $C_1(t)$ and $C_2(t)$ are the coupling strengths which can be tuned by gates $G_1$ and $G_2$. Following the proposal introduced in Sec. II, $C_{1(2)}(t) = \frac{1-\cos(\frac{t}{\tau}\pi)}{2}t_c$ when we turn off the gate $G_1$ ($G_2$), and $C_{1(2)}(t) = \frac{1+\cos(\frac{t}{\tau}\pi)}{2}t_c$ when we turn on the gate $G_1$ ($G_2$). In the numerical simulation of a realistic system, $t_c$ is set to a fixed value with $t_c = 0.23t_0$.

We should note there are three parameters, $t_1(t)$, $t_2(t)$, and $t_3(t)$, which are controlled by gates in the effective model of Eq. (2). However, only two parameters are needed in a realistic system since $t_1(t)$ and $t_2(t)$ are controlled by the same gate, $G_1$. After introducing the Hamiltonian, we apply the traditional time-evolution method using Trotter decomposition to compute the wave function. The wave function evolves according to $|\psi_i^\pm(t)\rangle = U(t)|\psi_i^\pm(0)\rangle$, where $U(t) = \hat{T} \exp[-\mathrm{i}\int_0^t dt' H_T(t')]$ is the time-evolution operator and $\hat{T}$ is the time-ordering operator [72]. $|\psi_i^\pm(0)\rangle = \frac{1}{\sqrt{2}}(u_{2i-1} \pm \mathrm{i}u_{2i})$ are the ground states of $H_{Si}$, which retain the same form as those in the effective model.

### A. Uniform nanowire with finite length

Here, we reveal how the braiding properties of MZMs are influenced by the length of the nanowire. In a uniform nanowire, the coupling energy of MZMs decreases exponentially with the increasing of the length of the nanowire. If the nanowire is not long enough, the two MZMs localized at the ends will inevitably hybridize. In Fig. 2(b), we plot the energy spectrum versus the magnetic field $B$ for a short nanowire, with its parameters indicated in the first row of Table I. The
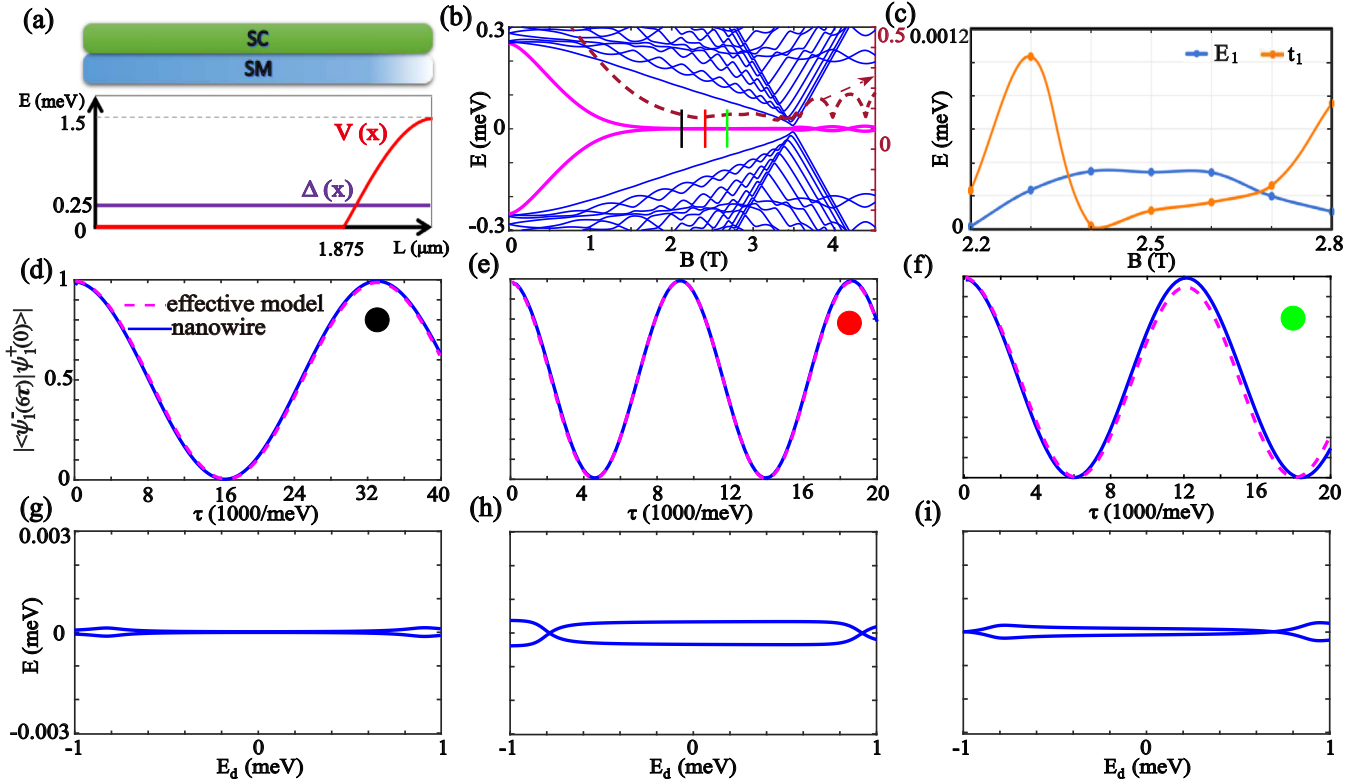
FIG. 4. Smooth inhomogeneous potential. (a) Schematic of the smooth inhomogeneous potential model, along with the corresponding distributions of $\Delta(x)$ and $V(x)$. (b) Energy spectrum of the smooth inhomogeneous potential model. Here, the energy of the ABSs are about one tenth of the value of the one in Fig. 3(b). However, $\eta$ is almost on the same order. (c) The value of $E_1$ and the corresponding effective $t_1$, focusing on the range from $B = 2.2$ T to $B = 2.8$ T. (d)–(f) Braiding results as a function of braiding time cost $\tau$ at different values of $B$, which are marked by the vertical lines in different colors in the energy spectrum in (b). The dashed line represents the fitting result from the effective model. (g)–(i) The corresponding energy spectrum of the quantum-dot–nanowire model as a function of $E_d$. In (d) and (g), $B = 2.2$ T, $E_1 = 1.547 \times 10^{-5}$ meV, and the corresponding effective $t_1 = 2.25 \times 10^{-4}$ meV. In (e) and (h), $B = 2.4$ T, $E_1 = 3.450 \times 10^{-4}$ meV, and the corresponding effective $t_1 = 2.00 \times 10^{-5}$ meV. In (f) and (i), $B = 2.8$ T, $E_1 = 1.036 \times 10^{-4}$ meV, and the corresponding effective $t_1 = 7.2 \times 10^{-4}$ meV. The other parameters are shown in the third row of Table I.

energy spectrum of MZMs is nearly zero energy when the system enters the topological region due to the finite-length effect. However, if we focus on a typical region range from $B = 2.25$ T to $B = 2.75$ T, the energy spectrum of MZMs actually oscillates around zero energy, as indicated by the blue line in Fig. 2(c). Following the proposal outlined in Sec. II, we investigate the braiding properties in this specific region. Figures 2(d)–2(f) show the final weight of $|\langle \psi_1^-(6\tau)|\psi_1^+(0)\rangle|$ versus the braiding time costing $\tau$ at $B = 2.25$ T, $B = 2.55$ T, and $B = 2.75$ T, respectively (indicated by the solid line). We can see that all the curves oscillate with $\tau$ due to the finite-size effect. What is more, the oscillation period is almost on the same order for $E_1 = 3.368 \times 10^{-5}$ meV at $B = 2.25$ T and for $E_1 = 4.885 \times 10^{-4}$ meV at $B = 2.75$ T. This is because $t_1$ also plays an important role during the braiding. The values of the effective $t_1$ are fitted through the effective model of Eq. (2). As indicated by the corresponding dashed lines in Figs. 2(d)–2(f), the final braiding results are well captured by the effective model. Interestingly, $t_1$ is closely related to $E_1$. As shown by the orange line in Fig. 2(c), the effective $t_1$ also oscillates around zero energy but with a different period. Since the total oscillation period is determined by the interplay of the effects induced by $E_1$ and $t_1$, the os-

cillation period of $|\langle \psi_1^-(6\tau)|\psi_1^+(0)\rangle|$ is almost on the same order.

This conclusion can be further confirmed through spectroscopic analysis. Reference [24] suggested that quantum dots at the ends of a nanowire can serve as a powerful tool to quantify the nonlocality of MZMs. Our proposal involves a structure with a coupled quantum-dot–nanowire system. In such a structure, if $E_1 \gg t_1$, the spectrum with respect to $E_d$ will display a bow-tie-like shape, while if $t_1 \gg E_1$, then the spectrum with respect to $E_d$ will display a diamond-like shape. Figures 2(g)–2(i) show the corresponding energy spectrum versus the on-site energy of the QD state $E_d$ with $C_1(t) = t_c$ and $C_2(t) = 0$. It indeed displays a bow-tie-like shape in Figs. 2(g) and 2(i). Here, $E_1$ is almost zero, while $t_1$ is very large. However, the spectrum displays a diamond-like shape in Fig. 2(i). Here, $t_1$ is almost zero, while $E_1$ is quite large. The spectrum is fully consistent with the braiding results.

Since $t_1$ is closely related to $E_1$, they both oscillate around zero energy with the same order of magnitude but with a different period. A plausible reason is that the MZMs are nonlocally distributed at the two ends of the nanowire. The MZMs that are far from the QD connect to the QD through
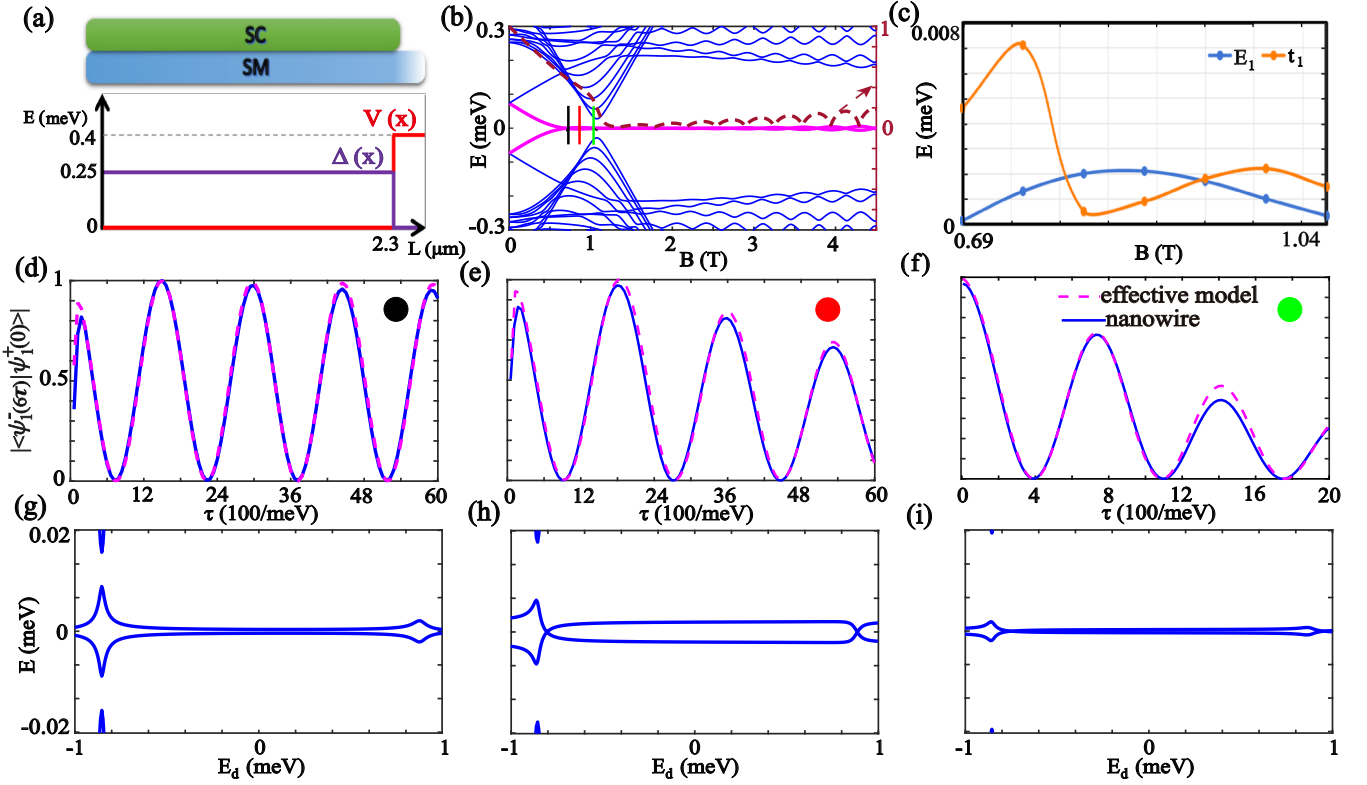
FIG. 5. Steplike quantum-dot structure. (a) Schematic plot of the steplike quantum-dot structure model. Here, $\Delta(x)$ is also inhomogeneous along the wire. (b) Energy spectrum of the steplike quantum-dot structure model, with the corresponding local estimator $\eta$ indicated by the dark red dashed line. (c) The value of $E_1$ and the corresponding effective $t_1$, focusing on the range from $B = 0.69$ T to $B = 1.065$ T. (d)–(f) Braiding results as a function of braiding time cost $\tau$ at different values of $B$, which are marked by the vertical lines in different colors in the energy spectrum in (b). The dashed line represents the fitting result from the effective model. (g)–(i) The corresponding energy spectrum of the quantum-dot–nanowire model as a function of $E_d$. In (d) and (g), $B = 0.6900$ T, $E_1 = 1.3569 \times 10^{-4}$ meV, and the corresponding effective $t_1 = 4.60 \times 10^{-3}$ meV. In (e) and (h), $B = 0.8775$ T, $E_1 = 2.1000 \times 10^{-3}$ meV, and the corresponding effective $t_1 = 9.00 \times 10^{-4}$ meV. In (f) and (i), $B = 1.0650$ T, $E_1 = 3.2964 \times 10^{-4}$ meV, and the corresponding effective $t_1 = 1.51 \times 10^{-3}$ meV. The other parameters are shown in the fourth row of Table I.

a finite length of the nanowire. We can expect that $t_1$ is also determined by the length of the nanowire, which is similar to $E_1$. Thus, it is reasonable that $E_1$ and $t_1$ are of the same order. Following Ref. [28], we can quantify the nonlocality of two MZMs through a parameter named the local estimator, $\eta = \sqrt{\frac{|u_2(x=L)|}{|u_1(x=L)|}}$. Here, $u_{1(2)}(x = L)$ is the normalized wave function of $\gamma_{1(2)}$ at the end. The dark red dashed line in Fig. 2(b) shows the corresponding curve of $\eta$ versus the magnetic field $B$. $\eta$ becomes very small when the system enters the topological region. This suggests that MZMs are indeed nonlocally distributed at the two ends of the nanowire. Therefore, for a long nanowire, $E_1$ is exponentially small in the topological region, and the corresponding $t_1$ will also be very small. In this situation, non-Abelian braiding will be sustained for a larger braiding time cost.

## B. Inhomogeneous potential at the boundary

We have revealed the braiding properties in a finite-size semiconductor-superconductor system. We now aim to further study the braiding properties of ABSs under various different conditions. First, we consider the case where the chemical

potential is inhomogeneous at the boundary. As shown in Fig. 3(a), the inhomogeneous chemical potential $V(x)$ (indicated by the red line) exhibits a steplike potential at the end, while the superconducting order parameter (indicated by the purple line) is uniform across the entire region. Since the ends or interfaces of a nanowire experience a different external field compared to the bulk, this case is quite common. As revealed by the energy spectrum in Fig. 3(b), the nearly zero energy states emerge before the system enters the topological region. The corresponding local estimator, indicated by the dark red dashed line in Fig. 3(b), is very large before the system enters the topological region. This suggests that the nearly zero energy states are confined within the inhomogeneous region and are not far from each other. Significantly, the braiding properties are not related to the local estimator. If we focus on the range from 1.4 to 1.9 T, these nearly zero energy states oscillate around zero energy, as indicated by the blue line in Fig. 3(c), while the orange solid line shows the corresponding effective value of $t_1$, which behaves similarly to the case with a finite length, regardless of the local estimator. Figures 3(d)–3(f) show the final weights of $|\langle \psi_1^-(6\tau)|\psi_1^+(0)\rangle|$ versus the time cost $\tau$ for $B = 1.4$ T, $B = 1.6$ T, and $B = 1.9$ T, respectively. The final braiding results oscillate almost on the same
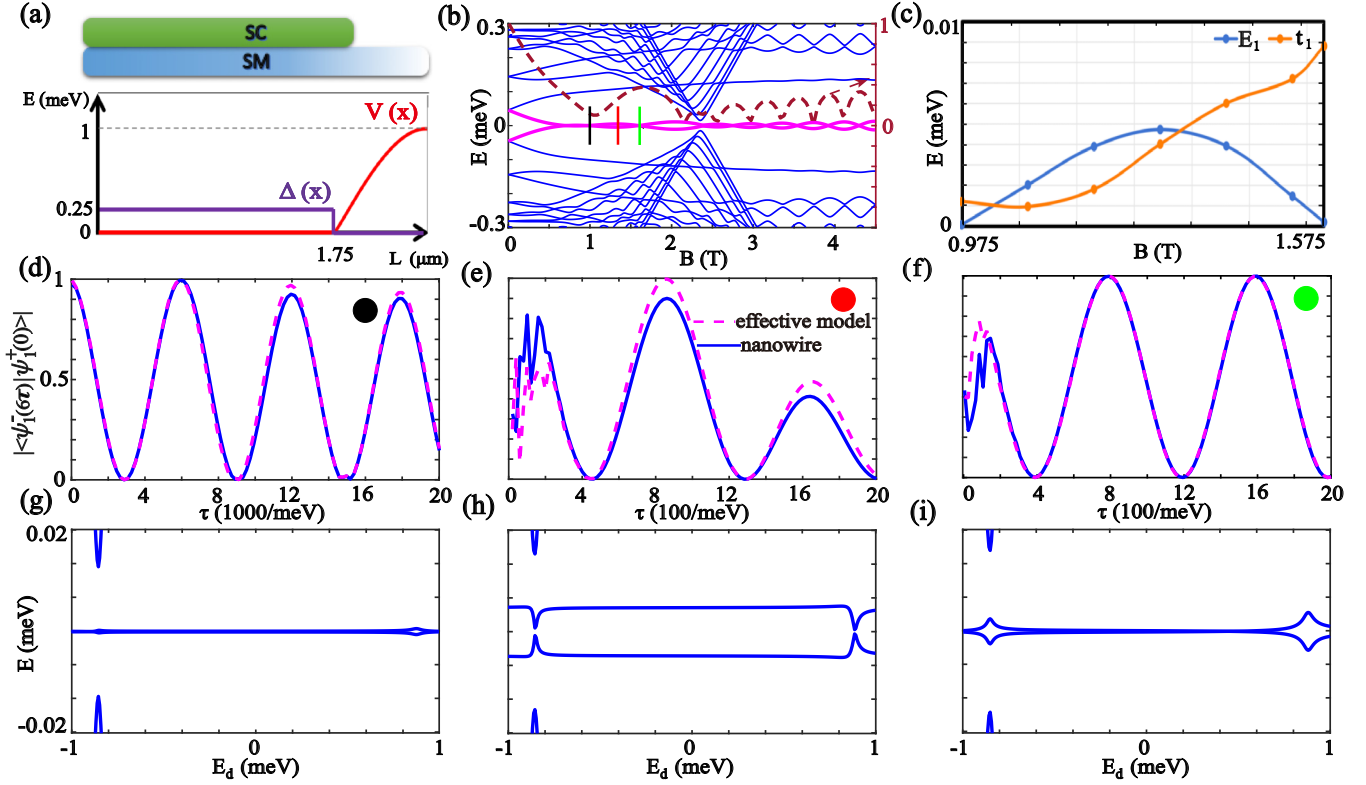
FIG. 6. Smooth quantum-dot structure. (a) Schematic plot of the smooth quantum-dot structure model. (b) Energy spectrum of the smooth quantum-dot structure model, with the corresponding local estimator $\eta$ indicated by the dark red dashed line. (c) The value of $E_1$ and the corresponding effective $t_1$, focusing on the range from $B = 0.975$ T to $B = 1.605$ T. (d)–(f) Braiding results as a function of braiding time cost $\tau$ at different values of $B$, which are marked by the vertical lines in different colors in the energy spectrum in (b). The dashed line represents the fitting result from the effective model. (g)–(i) The corresponding energy spectrum of the quantum-dot–nanowire model as a function of $E_d$. In (d) and (g), $B = 0.975$ T, $E_1 = 6.216 \times 10^{-5}$ meV, and the corresponding effective $t_1 = 1.20 \times 10^{-3}$ meV. In (e) and (h), $B = 1.320$ T, $E_1 = 4.717 \times 10^{-3}$ meV, and the corresponding effective $t_1 = 4.00 \times 10^{-3}$ meV. In (f) and (i), $B = 1.605$ T, $E_1 = 1.896 \times 10^{-4}$ meV, and the corresponding effective $t_1 = 8.80 \times 10^{-3}$ meV. The other parameters are shown in the fifth row of Table I.

order. This suggests that the braiding results are primarily related to $E_1$ and $t_1$. The corresponding energy spectrum versus the on-site energy of QD state $E_d$ at $C_1(t) = t_c$ and $C_2(t) = 0$ in Figs. 3(g)–3(i) is also consistent with the braiding results.

We further consider the case where the inhomogeneous potential $V(x)$ has a smooth spatial profile, as described by the parameters in the third row of Table I. In this situation, the energy spectrum of the quasi-MZM is closer to zero energy and about one tenth of that in the case where $V(x)$ is a step potential. Interestingly, the corresponding effective $t_1$ is of the same order as $E_1$, as indicated by the orange line in Fig. 4(c). The oscillation period of $|\langle \psi_1^-(6\tau)|\psi_1^+(0)\rangle|$, shown in Figs. 4(d)–4(f), also increases and becomes about 10 times greater than that in the case where $V(x)$ is a step potential. However, the local estimator indicated by the dark red dashed line in Fig. 4(c) remains the same as before. By comparing the braiding properties at two different energy scales $E_1$ while maintaining the same locality, we can observe that the braiding property is mainly associated with the stability of $E_1$. In other words, if the fluctuation amplitude of $E_1$ around zero energy is small, then the fluctuation amplitude of $t_1$ will also be small. Then the non-Abelian braiding will persist for a larger braiding time cost. The braiding properties of these nearly zero energy states behave similarly to those of two

coupled MZMs with finite length but with lower nonlocality. A possible reason might be related to the spin degrees of freedom of MZMs in a nanowire. Wimmer and colleagues demonstrated that two MZMs with finite overlap have opposite spins. Consequently, these two MZMs will experience different tunnel barriers when traversing an inhomogeneous potential. This results in an exponential difference in the coupling between the two MZMs and the environment [29]. Our braiding results are fully consistent with this theory.

### C. Quantum-dot-like structure at the boundary

Since superconductivity is induced through the proximity effect in a nanowire-superconductor hybrid system, it is likely that superconductivity is weakened at the interface. In this scenario, both the chemical potential and the superconducting amplitude are inhomogeneous at the interface. This creates an additional quantum-dot-like structure at the boundary. Consequently, subgap states may form due to this quantum-dot structure. Such subgap states could evolve into nearly zero energy states with the variation of the magnetic field under certain conditions. In Fig. 5(b), the energy spectrum displays a nearly zero energy state before the system enters the topological region with the parameters shown in the fourth row
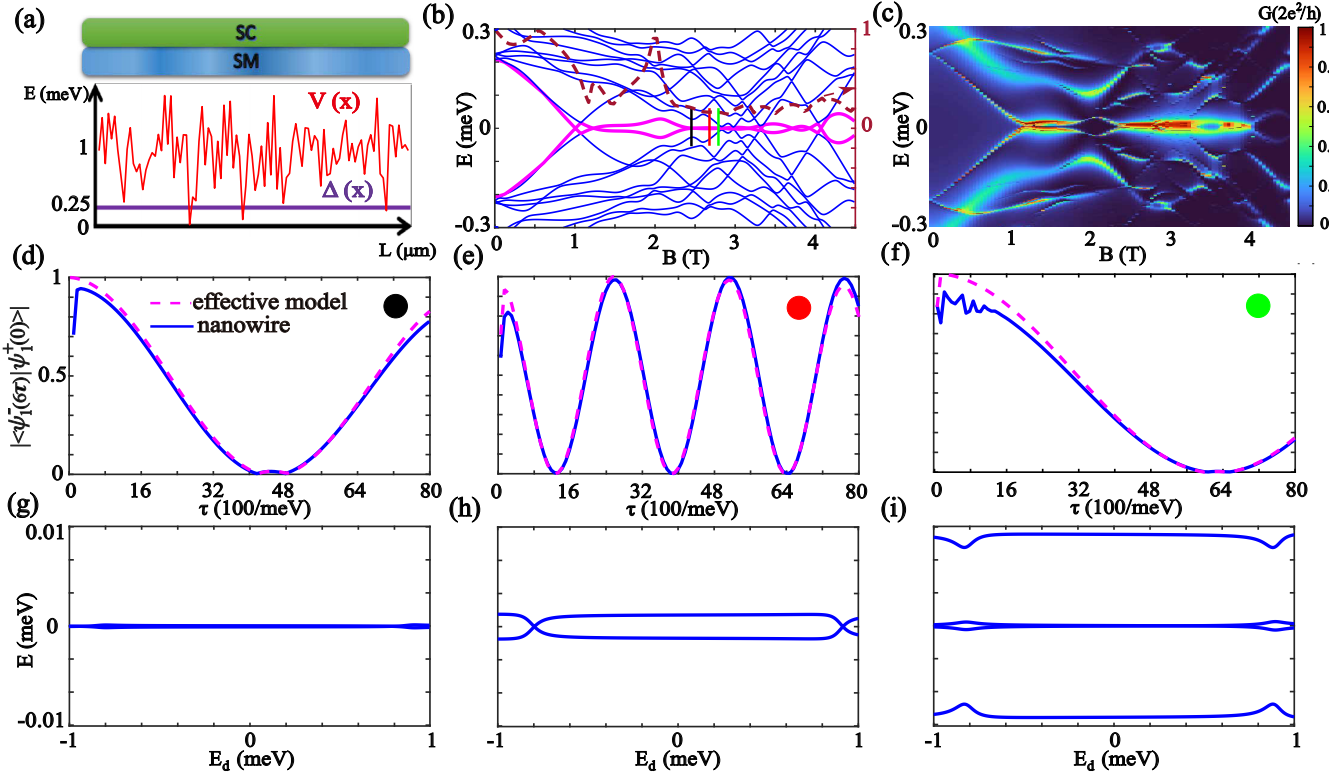
FIG. 7. Disorder. (a) A schematic plot of the disorder model is shown in the top panel. $V(x)$ is randomly distributed along the nanowire. (b) Energy spectrum and the corresponding local estimator $\eta$. (c) Differential conductance as a function of $E$ and $B$. Here, ZBPs are not consistent with the spectrum due to the influence of disorder. (d)–(f) Braiding results as a function of braiding time cost $\tau$ at different values of $B$, marked by the vertical lines in different colors in (b) and displaying displaying ZBPs in (c). The dashed line represents the fitting result from the effective model. (g)–(i) The corresponding energy spectrum of the quantum-dot–nanowire model as a function of $E_d$. In (d) and (g), $B = 2.484$ T, $E_1 = 5.593 \times 10^{-5}$ meV, and the corresponding effective $t_1 = 4 \times 10^{-4}$ meV. In (e) and (h), $B = 2.715$ T, $E_1 = 1.200 \times 10^{-3}$ meV, and the corresponding effective $t_1 = 2 \times 10^{-4}$ meV. In (f) and (i), $B = 2.807$ T, $E_1 = 2.247 \times 10^{-5}$ meV, and the corresponding effective $t_1 = 5 \times 10^{-4}$ meV. The other parameters are shown in the sixth row of Table I.

of Table I. Figures 5(d)–5(f) show the corresponding braiding results $|\langle \psi_1^-(6\tau)|\psi_1^+(0)\rangle|$ versus braiding time cost $\tau$. Clearly, the braiding results oscillate with $\tau$ and are well captured by the effective model. We further quantify the corresponding $t_1$ using the effective model, with the data indicated by the orange line in Fig. 5(c). The behavior of the nearly zero energy states remains consistent with previous observations. The corresponding $E_1$ and $t_1$ fluctuate around zero energy and effectively compensate each other. As a result, the oscillation period of $|\langle \psi_1^-(6\tau)|\psi_1^+(0)\rangle|$ is nearly the same order within a finite range and is determined by the stability of $E_1$.

We also consider a quantum-dot structure where the chemical potential is spatially smooth. The corresponding parameters are provided in the fifth line of Table 1. As shown in Fig. 6, the oscillation period of $|\langle \psi_1^-(6\tau)|\psi_1^+(0)\rangle|$ is still determined by the stability of $E_1$. There is no significant difference regardless of whether the chemical potential spatially varies rapidly or smoothly. This suggests that the nearly zero energy states in a quantum-dot-like structure can also be attributed to finite coupled MZMs. The nearly zero energy ABSs in a quantum-dot-like structure might also be utilized for quantum computation if the fluctuation of $E_1$ is small. However, stabilizing ABSs in such a structure is more challenging than the cases where only the chemical potential is inhomogeneous.

### D. Disorder at the bulk

In state-of-the-art of nanotechnology, disorder inevitably occurs in nanowire systems. Since the first semiconductor-superconductor nanowires were fabricated experimentally in 2012, this issue has attracted significant attention. Theoretical and experimental studies suggest that disorder can lead to the collapse of bulk states and induce similar ZBPs in experiments in experiments. Although disorder has been largely suppressed and quantized ZBPs have been observed experimentally over the past decade, theory suggests that quantized ZBPs may still be detected in trivial situations under the influence of disorder. Here, we investigate the braiding properties of MZMs in the presence of disorder. We focus mainly on the ABSs, which can cause quantized ZBPs in the conductance measurement. Figure 7(b), a typical energy spectrum resulting from disorder is shown. In this case, $V(x)$ is a random potential represented by an uncorrelated Gaussian distribution, i.e., $V(x) \sim \mathcal{N}(0, 1^2)$, where $V(x) \sim \mathcal{N}(0, 1^2)$ denotes a Gaussian distribution with a mean value of 0 and variance of 1. Figure 7(c) displays the corresponding differential conductance as a function of magnetic field and voltage. We observe that a quantized ZBP appears within a specific range. The range of the quantized ZBPs is not fully consistent with the spectrum because some of the nearly zero energy ABSs are confined
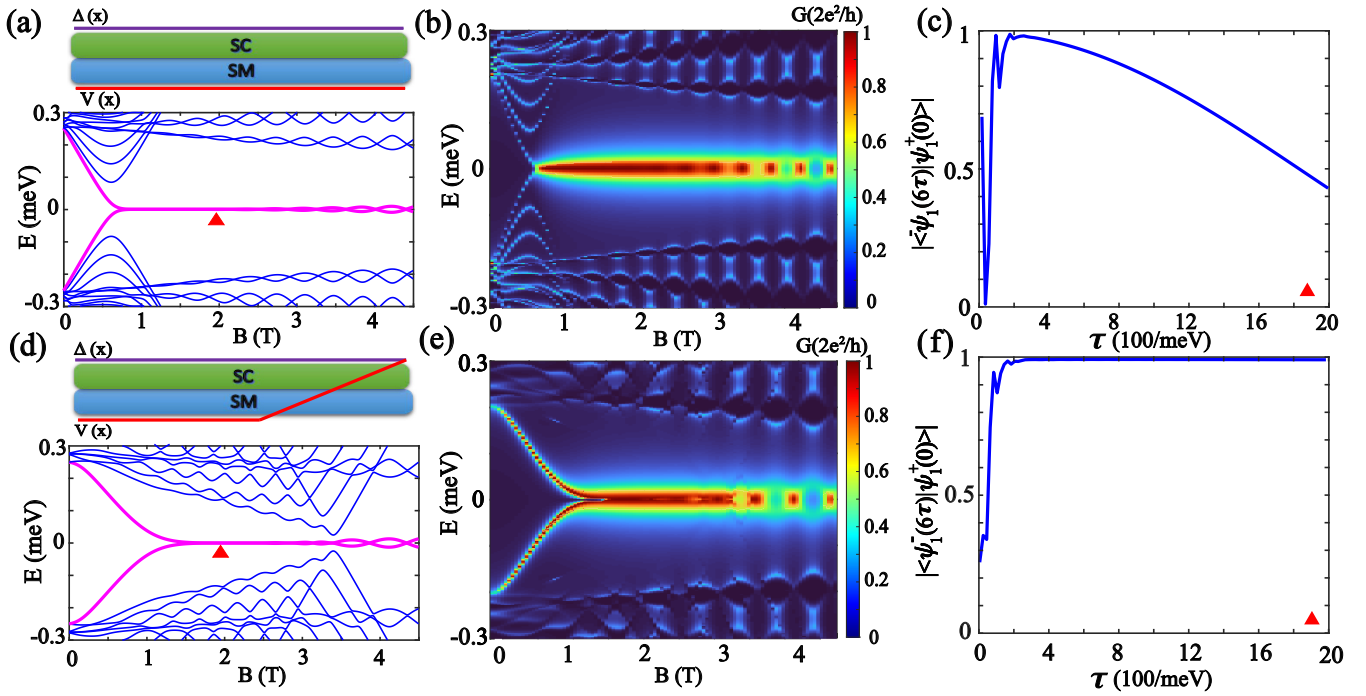
FIG. 8. (a) Schematic plot of a uniform nanowire and the corresponding energy spectrum. (d) Schematic plot of an inhomogeneous potential and the corresponding energy spectrum. Both models display zero-bias conductance peaks, as shown in (b) and (e), respectively. (c) and (f) The braiding results as a function of braiding time cost at the magnetic field $B = 1.9$ T, indicated by the red triangles in (a) and (d). We observe that the non-Abelian braiding fidelity is significantly enhanced in the case of the inhomogeneous potential.

within the bulk region due to disorder. Here, we focus on the range where ZBPs can be detected. Figures 7(d)–7(f) show $|\langle \psi_1^-(6\tau)|\psi_1^+(0)\rangle|$ versus the time cost $\tau$ at some typical position. Interestingly, we find that these ABSs exhibit behavior similar to that of finite-overlap MZMs. Their properties are

influenced by the interplay between the effects induced by $E_1$ and $t_1$. Moreover, $t_1$ is also related to $E_1$, and they both oscillate, with their oscillation periods being almost the same order. This further suggests that the stability of non-Abelian braiding is mainly determined by the stability of $E_1$. To show
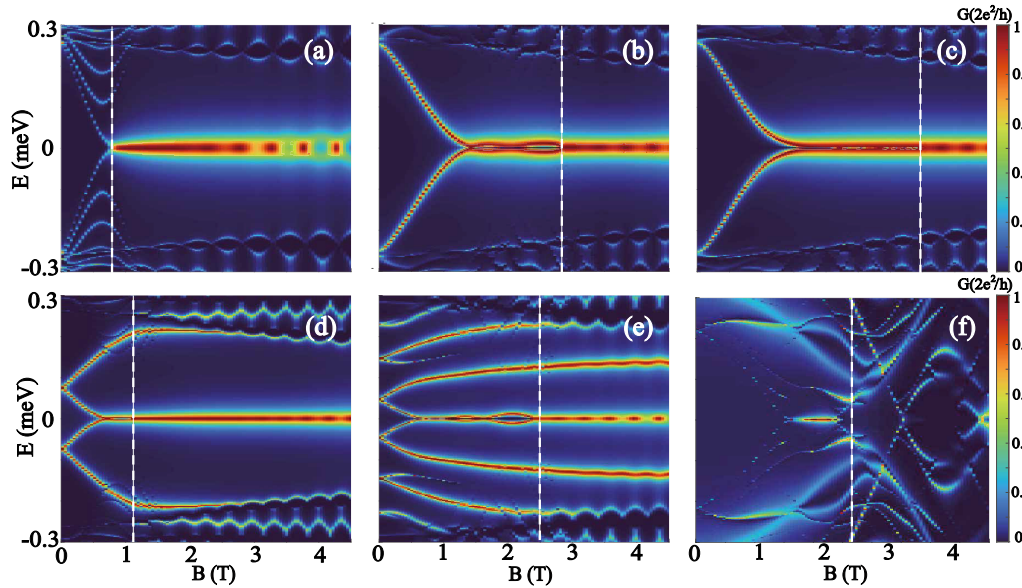


FIG. 9. Tunneling conductance. The white dashed lines denote the point of the topological quantum phase transition. (a) Uniform nanowire with finite length. (b) Nanowire with a steplike inhomogeneous potential at the boundary. (c) Nanowire with a smooth inhomogeneous potential at the boundary. (d) Nanowires with a steplike quantum-dot-like structure at the boundary. (e) Nanowires with a smooth quantum-dot-like structure at the boundary. (f) Nanowire with disorder at the bulk. The other parameters are shown in Table I.

the generality of this conclusion, we calculate another configuration of disorder; the results are presented in Appendix C. This suggests that these nearly zero energy states may also originate from the inhomogeneous potential at the interface. Disorder could induce a local potential profile that behaves similarly to the inhomogeneous potential at the interface. Consequently, the ABSs induced by disorder behave similarly to those found in the presence of an inhomogeneous potential.

### E. Non-Abelian braiding modified by the inhomogeneous potential

We have revealed that these nearly zero energy ABSs, despite their differing mechanisms, exhibit properties similar to those of finite-overlap MZMs. Their non-Abelian braiding property will gradually be destroyed by additional $E_1$ and $t_1$. Since $t_1$ is also related to $E_1$, the primary criterion is actually the stability of $E_1$ near zero energy. If $E_1$ fluctuates with a vanishingly small amplitude around zero energy, the oscillation period of the braiding results will be quite large. In this situation, if the braiding process is completed with $\tau \ll 1/E_1$, the dynamical effects can be neglected, leading to high fidelity in the braiding. This suggests that these nearly zero energy ABSs might still be used for non-Abelian braiding if we can stabilize $E_1$ at zero energy. Experimentally, the typical length of a nanowire is about 2 μm. Figure 8(a) shows the corresponding energy spectrum of a nanowire of this length as a function of the magnetic field. In such a clean nanowire system, it will enter the topological region if $B > 1$ T. The differential conductance in Fig. 8(b) exhibits a clear quantized ZBP in the topological region. We further investigate the non-Abelian braiding properties of MZMs at $B = 1.9$ T. Although swapping is successful if the time cost $\tau$ is short, Fig. 8(c) reveals that deviations from perfect swapping occur as $\tau$ increases, eventually leading to oscillations with $\tau$. Interestingly, if we introduce an inhomogeneous potential at the interface while keeping other parameters unchanged, quasi-Majorana zero modes (quasi-MZMs) will emerge, as shown in Fig. 8(d). These quasi-MZMs will also induce stable quantized ZBPs in the differential conductance [32–34,67]. Moreover, the non-Abelian braiding fidelity is significantly enhanced in this situation. Figure 8(f) demonstrates that perfect swapping can be sustained for larger braiding time cost without any deviation. This suggests that these nearly zero energy ABSs may also be suitable for topological quantum computation.

### IV. CONCLUSION

We systemically investigated the braiding properties of ABSs induced by various inhomogeneous potentials in a nanowire. We found that these ABSs can be considered MZMs with finite overlap. These finite-overlap MZMs introduce additional coupling terms $E_1$ and $t_1$, which lead to dynamical effects and deviations from the non-Abelian braiding properties of MZMs. The numerical simulations are in good agreement with the effective model. Moreover, the deviation is influenced by the stability of $E_1$ within a certain range. In other words, if $E_1$ remains at zero energy with a vanishingly small fluctuation, the non-Abelian braiding properties

will remain over an extended range. Indeed, we found the non-Abelian braiding of ABSs under certain conditions can outperform that of MZMs in realistic systems. This suggests that ABSs may also be suitable for quantum computation.

Finally, we want to emphasize that quantized ZBPs could still be a valuable tool for distinguishing MZMs. The braiding properties of ABSs suggest that these nearly zero energy states may be attributed to finite-overlap MZMs. The non-Abelian braiding property of these nearly zero energy states can remain stable for a larger braiding time cost if the fluctuation of $E_1$ around zero energy is tiny. This implies that if quantized ZBPs are observed across a certain range, then this range could be a promising platform for non-Abelian braiding. To further quantify the stability of these ABSs, additional operations such as performing the braiding and fusion protocols may be required.

### APPENDIX A: LOCAL ESTIMATOR $\eta$

Consider a general subgap eigenstate in a nanowire system:

$$d = \int dx \sum_\sigma u_\sigma(x)\psi_\sigma(x) + v_\sigma(x)\psi_\sigma^\dagger(x). \quad \text{(A1)}$$

Here, $u_\sigma(x)$ and $v_\sigma(x)$ are the probability amplitudes of the particle and hole wave functions. $\sigma$ is the spin projection. We can decompose this fermion state into Majorana components $\gamma_1$ and $\gamma_2$:

$$d = \frac{\gamma_1 + i\gamma_2}{\sqrt{2}},$$
$$d^\dagger = \frac{\gamma_1 - i\gamma_2}{\sqrt{2}}, \quad \text{(A2)}$$

so that $\gamma_{1(2)} = \int dx \sum_\sigma u_{\sigma,1(2)}(x)\psi_\sigma(x) + [u_{\sigma,1(2)}(x)]^*\psi_\sigma^\dagger(x)$. $\gamma_{1(2)}$ is self-conjugate. The probability amplitude of $\gamma_{1(2)}$ can be written as

$$u_1(x) = \sum_\sigma \frac{u_\sigma(x) + v_\sigma^*(x)}{\sqrt{2}},$$
$$u_2(x) = \sum_\sigma \frac{u_\sigma(x) - v_\sigma^*(x)}{i\sqrt{2}}. \quad \text{(A3)}$$

Thus, we can define the local estimator $\eta$:

$$\eta = \sqrt{\frac{|u_2(x = L)|}{|u_1(x = L)|}}. \quad \text{(A4)}$$

### APPENDIX B: TUNNELING CONDUCTANCE

To simulate the experimental measurement of the tunneling conductance $G$, we attach a normal lead to the end of the nanowire and numerically calculate the tunneling
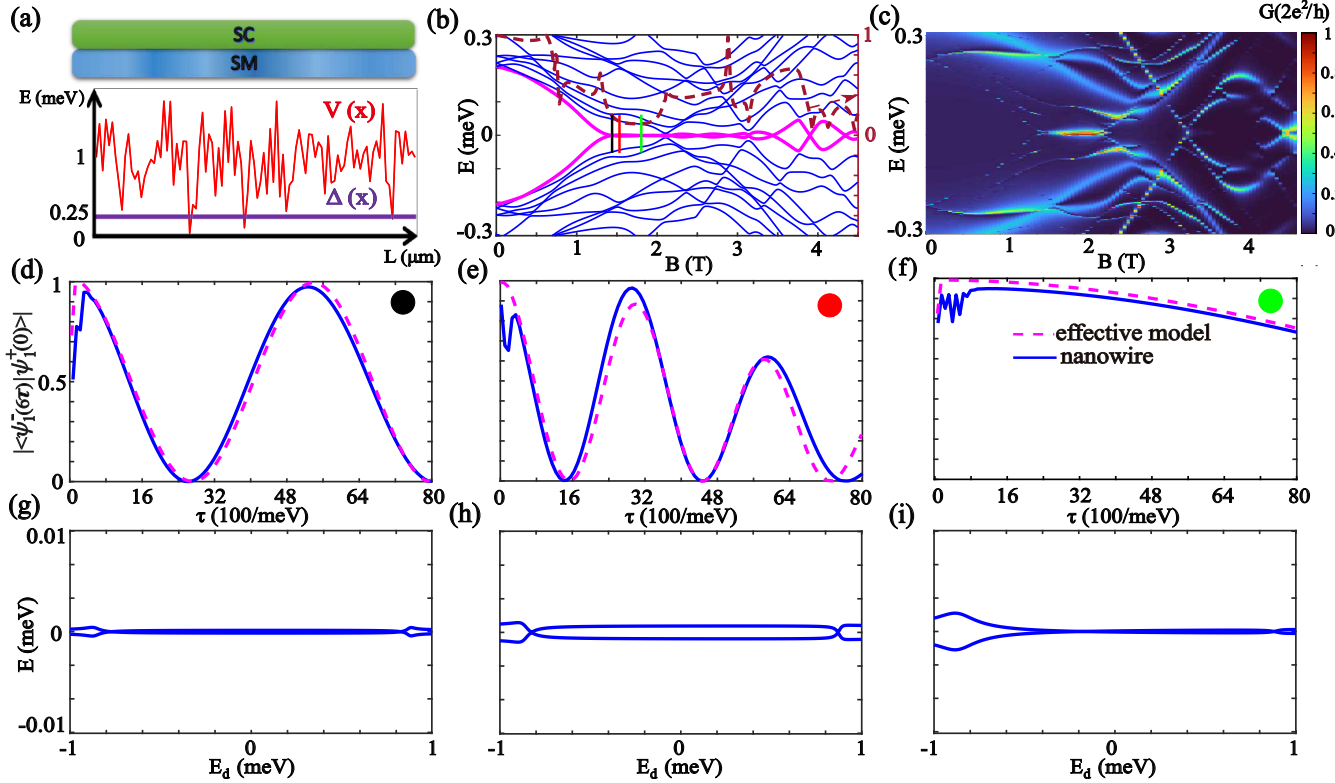
FIG. 10. Disorder with another configuration. (a) A schematic plot of the disorder model is shown in the top panel. (b) Energy spectrum and the corresponding local estimator $\eta$. (c) Differential conductance as a function of $E$ and $B$. (d)–(f) Braiding results as a function of braiding time cost $\tau$ for different values of $B$, marked by the vertical lines in different colors in (b) and displaying zero-bias peaks in (c). The dashed line represents the fitting result from the effective model. (g)–(i) The energy spectrum of the dot-nanowire model as a function of the on-site QD state $E_d$ for different $B$. In (b) and (e), $B_x = 1.84$ T, $E_1 = 7.88 \times 10^{-5}$ meV, and $t_1 = 1.4 \times 10^{-3}$ meV. In (c) and (f), $B_x = 1.93$ T, $E_1 = 6.71 \times 10^{-4}$ meV, and $t_1 = 3.5 \times 10^{-3}$ meV . In (d) and (g), $B_x = 2.02$ T, $E_1 = 5.75 \times 10^{-5}$ meV, and $t_1 = 2.5 \times 10^{-4}$ meV. The other parameters are shown in the sixth row of Table I.

conductance using the nonequilibrium Green's function:

$$\mathbf{G}^r(\epsilon) = 1 \bigg/ \left[ \epsilon \mathbf{I} - \mathbf{H}_s - \sum_m \mathbf{\Sigma}_m^r \right]. \tag{B1}$$

In the Nambu representation, the Green's function can be divided into $\mathbf{G}^r = [G_{ee}^r, G_{eh}^r; G_{he}^r, G_{hh}^r]$. $G_{ee}^r$, $G_{hh}^r$, and $G_{eh}^r$ are the electron part, hole part, and joint electron-hole part matrix elements of $\mathbf{G}^r$, respectively. In addition, $\mathbf{G}_{ji}^a = (\mathbf{G}_{ij}^r)^\dagger$, and the self-energy due to the leads satisfies the relation

$$\mathbf{\Gamma}_m(\epsilon) = i \big[ \mathbf{\Sigma}_m^r(\epsilon) - \mathbf{\Sigma}_m^a(\epsilon) \big]. \tag{B2}$$

$\Gamma_m$ is the linewidth function of the normal leads. In the subsequent calculation, we set the linewidth function to a constant and stick to zero temperature. Once the Green's function is obtained, we can calculate the conductance through the transmission coefficient:

$$T_{nm}(\epsilon) = \text{Tr} \left[ \Gamma_n \mathbf{G}^r \Gamma_m \mathbf{G}^a \right]. \tag{B3}$$

Figure 9 shows the corresponding tunneling conductance in various situations. If the ABSs are unstable at zero energy, the conductance peak will deviate from zero energy soon and show only a cross at zero energy. However, if the ABSs are close to zero energy with little fluctuation, they display the signature of quantized zero-bias conductance peaks within a range. This implies that if quantized ZBPs are observed across a certain range, then this range could be a promising platform for non-Abelian braiding. To further quantify the stability of these ABSs, additional operations such as performing the braiding and fusion protocols may be required.

## APPENDIX C: DISORDER AT THE BULK

We calculate another configuration of disorder; the results are the same as before. Figures 10(b)–10(d) show $|\langle \psi_1^-(6\tau)|\psi_1^+(0)\rangle|$ versus the braiding time cost $\tau$ at some typical position. These ABSs exhibit behavior similar to that of finite-overlap MZMs. Their properties are influenced by the interplay between the effects induced by $E_1$ and $t_1$. $t_1$ is also related to $E_1$, and they both oscillate with almost the same order of oscillation period.

[1] J. D. Sau, R. M. Lutchyn, S. Tewari, and S. Das Sarma, Generic new platform for topological quantum computation using semiconductor heterostructures, Phys. Rev. Lett. **104**, 040502 (2010).

[2] S. Fujimoto, Topological order and non-Abelian statistics in noncentrosymmetric $s$-wave superconductors, Phys. Rev. B **77**, 220501(R) (2008).

[3] M. Sato, Y. Takahashi, and S. Fujimoto, Non-Abelian topological orders and Majorana fermions in spin-singlet superconductors, Phys. Rev. B **82**, 134521 (2010).

[4] J. Alicea, Majorana fermions in a tunable semiconductor device, Phys. Rev. B **81**, 125318 (2010).

[5] R. M. Lutchyn, J. D. Sau, and S. Das Sarma, Majorana fermions and a topological phase transition in semiconductor-superconductor heterostructures, Phys. Rev. Lett. **105**, 077001 (2010).

[6] V. T. Phong, H. Sainz-Cruz, E. J. Mele, and F. Guinea, Mirror-protected Majorana zero modes in $f$-wave multilayer graphene superconductors, Phys. Rev. B **110**, L100501 (2024).

[7] V. T. Phong, N. R. Walet, and F. Guinea, Majorana zero modes in a two-dimensional $p$-wave superconductor, Phys. Rev. B **96**, 060505(R) (2017).

[8] Y. Tanaka, T. Yokoyama, and N. Nagaosa, Manipulation of the Majorana fermion, Andreev reflection, and Josephson current on topological insulators, Phys. Rev. Lett. **103**, 107002 (2009).

[9] V. Mourik, K. Zuo, S. M. Frolov, S. R. Plissard, E. P. A. M. Bakkers, and L. P. Kouwenhoven, Signatures of Majorana fermions in hybrid superconductor-semiconductor nanowire devices, Science **336**, 1003 (2012).

[10] M. T. Deng, C. L. Yu, G. Y. Huang, M. Larsson, P. Caroff, and H. Q. Xu, Anomalous zero-bias conductance peak in a Nb-InSb nanowire-Nb hybrid device, Nano Lett. **12**, 6414 (2012).

[11] A. Das, Y. Ronen, Y. Most, Y. Oreg, M. Heiblum, and H. Shtrikman, Zero-bias peaks and splitting in an Al-InAs nanowire topological superconductor as a signature of Majorana fermions, Nat. Phys. **8**, 887 (2012).

[12] Ö. Gül, H. Zhang, J. D. S. Bommer, M. W. A. de Moor, D. Car, S. R. Plissard, E. P. A. M. Bakkers, A. Geresdi, K. Watanabe, T. Taniguchi, and L. P. Kouwenhoven, Ballistic Majorana nanowire devices, Nat. Nanotechnol. **13**, 192 (2018).

[13] S. M. Albrecht, A. P. Higginbotham, M. Madsen, F. Kuemmeth, T. S. Jespersen, J. Nygard, P. Krogstrup, and C. M. Marcus, Exponential protection of zero modes in Majorana islands, Nature (London) **531**, 206 (2016).

[14] M. T. Deng, S. Vaitiekenas, E. B. Hansen, J. Danon, M. Leijnse, K. Flensberg, J. Nygård, P. Krogstrup, and C. M. Marcus, Majorana bound state in a coupled quantum-dot hybrid-nanowire system, Science **354**, 1557 (2016).

[15] S. Nadj-perge, I. K. Drozdov, J. Li, H. Chen, S. Jeon, J. Seo, A. H. MacDonald, B. Andrei Bernevig, and A. Yazdani, Observation of Majorana fermions in ferromagnetic atomic chains on a superconductor, Science **346**, 602 (2014).

[16] B. E. Feldman, M. T. Randeria, J. Li, S. Jeon, Y. Xie, Z. Wang, I. K. Drozdov, B. Andrei Bernevig, and A. Yazdani, High-resolution studies of the Majorana atomic chain platform, Nat. Phys. **13**, 286 (2017).

[17] A. Fornieri, A. M. Whiticar, F. Setiawan, E. Portolés, A. C. C. Drachmann, A. Keselman, S. Gronin, C. Thomas, T. Wang, R. Kallaher, G. C. Gardner, E. Berg, M. J. Manfra, A. Stern, C. M. Marcus, and F. Nichele, Evidence of topological superconduc-tivity in planar Josephson junctions, Nature (London) **569**, 89 (2019).

[18] H. Ren, F. Pientka, S. Hart, A. Pierce, M. Kosowsky, L. Lunczer, R. Schlereth, B. Scharf, E. M. Hankiewicz, L. W. Molenkamp, B. I. Halperin, and A. Yacoby, Topological superconductivity in a phase-controlled Josephson junction, Nature (London) **569**, 93 (2019).

[19] Z. Wang, H. Song, D. Pan, Z. Zhang, W. Miao, R. Li, Z. Cao, G. Zhang, L. Liu, L. Wen, R. Zhuo, D. E. Liu, K. He, R. Shang, J. Zhao, and H. Zhang, Plateau regions for zero-bias peaks within 5% of the quantized conductance value $2e^2/h$, Phys. Rev. Lett. **129**, 167702 (2022).

[20] L. Kouwenhoven, Perspective on Majorana bound-states in hybrid superconductor-semiconductor nanowires, Modern Phys. Lett. B **39**, 2540002 (2025).

[21] J. Liu, A. C. Potter, K. T. Law, and P. A. Lee, Zero-bias peaks in the tunneling conductance of spin-orbit-coupled superconducting wires with and without Majorana end-states, Phys. Rev. Lett. **109**, 077205 (2012).

[22] G. Kells, D. Meidan, and P. W. Brouwer, Near-zero-energy end states in topologically trivial spin-orbit coupled superconducting nanowires with a smooth confinement, Phys. Rev. B **86**, 100503(R) (2012).

[23] E. Prada, P. San-Jose, and R. Aguado, Transport spectroscopy of $NS$ nanowire junctions with Majorana fermions, Phys. Rev. B **86**, 180503(R) (2012).

[24] E. Prada, R. Aguado, and P. San-Jose, Measuring Majorana nonlocality and spin structure with a quantum dot, Phys. Rev. B **96**, 085418 (2017).

[25] C. Fleckenstein, F. Dominguez, N. Traverso Ziani, and B. Trauzettel, Decaying spectral oscillations in a Majorana wire with finite coherence length, Phys. Rev. B **97**, 155425 (2018).

[26] C. Moore, T. D. Stanescu, and S. Tewari, Two-terminal charge tunneling: Disentangling Majorana zero modes from partially separated Andreev bound states in semiconductor-superconductor heterostructures, Phys. Rev. B **97**, 165302 (2018).

[27] C.-X. Liu, J. D. Sau, and S. Das Sarma, Distinguishing topological Majorana bound states from trivial Andreev bound states: Proposed tests through differential tunneling conductance spectroscopy, Phys. Rev. B **97**, 214502 (2018).

[28] F. Penaranda, R. Aguado, P. San-Jose, and E. Prada, Quantifying wave-function overlaps in inhomogeneous Majorana nanowires, Phys. Rev. B **98**, 235406 (2018).

[29] A. Vuik, B. Nijholt, A. R. Akhmerov, and M. Wimmer, Reproducing topological properties with quasi-Majorana states, SciPost Phys. **7**, 061 (2019).

[30] T. D. Stanescu and S. Tewari, Robust low-energy Andreev bound states in semiconductor-superconductor structures: Importance of partial separation of component Majorana bound states, Phys. Rev. B **100**, 155429 (2019).

[31] C.-X. Liu, J. D. Sau, T. D. Stanescu, and S. Das Sarma, Andreev bound states versus Majorana bound states in quantum dot-nanowire-superconductor hybrid structures: Trivial versus topological zero-bias conductance peaks, Phys. Rev. B **96**, 075161 (2017).

[32] F. Setiawan, C.-X. Liu, J. D. Sau, and S. Das Sarma, Phenomenology of the soft gap, zero-bias peak, and zero-mode splitting in ideal Majorana nanowires, Phys. Rev. B **96**, 184520 (2017).

[33] C.-K. Chiu and S. Das Sarma, Fractional Josephson effect with and without Majorana zero modes, Phys. Rev. B **99**, 035312 (2019).

[34] C. Moore, C. C. Zeng, T. D. Stanescu, and S. Tewari, Quantized zero-bias conductance plateau in semiconductor-superconductor heterostructures without topological Majorana zero modes, Phys. Rev. B **98**, 155314 (2018).

[35] Z. Cao, G. Zhang, H. Zhang, W. X. He, C. C. Zeng, K. He, and D. E. Liu, Probing electron-hole weights of an Andreev bound state by transient currents, Phys. Rev. B **106**, 075416 (2022).

[36] P. Marra and A. Nigro, Majorana/Andreev crossover and the fate of the topological phase transition in inhomogeneous nanowires, J. Phys.: Condens. Matter **34**, 124001 (2022).

[37] F. Chi, J. Wang, T. Y. He, Z. G. Fu, P. Zhang, X. W. Zhang, L. H. Wang, and Z. L. Lu, Quantum interference effects in quantum dot molecular with Majorana bound states, Front. Phys. **8**, 631031 (2021).

[38] H. Y. Tian and C. D. Ren, Distinguishing Majorana and quasi-Majorana bound states in a hybrid superconductor-semiconductor nanowire with inhomogeneous potential barriers, Results Phys. **26**, 104273 (2021).

[39] Y. Asano, Y. Tanaka, A. A. Golubov, and S. Kashiwaya, Conductance spectroscopy of spin-triplet superconductors, Phys. Rev. Lett. **99**, 067005 (2007).

[40] R. V. Mishmash, D. Aasen, A. P. Higginbotham, and J. Alicea, Approaching a topological phase transition in Majorana nanowires, Phys. Rev. B **93**, 245404 (2016).

[41] J. Liu, J. T. Song, Q. F. Sun, and X. C. Xie, Even-odd interference effect in a topological superconducting wire, Phys. Rev. B **96**, 195307 (2017).

[42] T. O. Rosdahl, A. Vuik, M. Kjaergaard, and A. R. Akhmerov, Andreev rectifier: A nonlocal conductance signature of topological phase transitions, Phys. Rev. B **97**, 045421 (2018).

[43] J. Cayao, E. Prada, P. San-Jose, and R. Aguado, SNS junctions in nanowires with spin-orbit coupling: Role of confinement and helicity on the subgap spectrum, Phys. Rev. B **91**, 024514 (2015).

[44] J. Danon, A. B. Hellenes, E. B. Hansen, L. Casparis, A. P. Higginbotham, and K. Flensberg, Nonlocal conductance spectroscopy of Andreev bound states: Symmetry relations and BCS charges, Phys. Rev. Lett. **124**, 036801 (2020).

[45] G. C. Ménard, G. L. R. Anselmetti, E. A. Martinez, D. Puglia, F. K. Malinowski, J. S. Lee, S. Choi, M. Pendharkar, C. J. Palmstrom, K. Flensberg, C. M. Marcus, L. Casparis, and A. P. Higginbotham, Conductance-matrix symmetries of a three-terminal hybrid device, Phys. Rev. Lett. **124**, 036802 (2020).

[46] H. Zhang, D. E. Liu, M. Wimmer, and L. P. Kouwenhoven, Next steps of quantum transport in Majorana nanowire devices, Nat. Commun. **10**, 5128 (2019).

[47] K. Yavilberg, E. Ginossar, and E. Grosfeld, Differentiating Majorana from Andreev bound states in a superconducting circuit, Phys. Rev. B **100**, 241408(R) (2019).

[48] A. Ptok, A. Kobialka, and T. Domanski, Controlling the bound states in a quantum-dot hybrid nanowire, Phys. Rev. B **96**, 195430 (2017).

[49] O. A. Awoga, J. Cayao, and A. M. Black-Schaffer, Supercurrent detection of topologically trivial zero-energy states in nanowire junctions, Phys. Rev. Lett. **123**, 117001 (2019).

[50] C. Reeg, O. Dmytruk, D. Chevallier, D. Loss, and J. Klinovaja, Zero-energy Andreev bound states from quantum dots in proximitized Rashba nanowires, Phys. Rev. B **98**, 245407 (2018).

[51] D. I. Pikulin, B. van Heck, T. Karzig, E. A. Martinez, B. Nijholt, T. Laeven, G. W. Winkler, J. D. Watson, S. Heedt, M. Temurhan, V. Svidenko, R. M. Lutchyn, M. Thomas, G. de Lange, L. Casparis, and C. Nayak, Protocol to identify a topological superconducting phase in a three-terminal device, arXiv:2103.12217.

[52] M. Aghaee *et al.* (Microsoft Quantum), InAs-Al hybrid devices passing the topological gap protocol, Phys. Rev. B **107**, 245423 (2023).

[53] Y. Tanaka, S. Tamura, and J. Cayao, Theory of Majorana zero modes in unconventional superconductors, Prog. Theor. Exp. Phys. **8**, 08C105 (2024).

[54] R. Hess, H. F. Legg, D. Loss, and J. Klinovaja, Trivial Andreev band mimicking topological bulk gap reopening in the nonlocal conductance of long Rashba nanowires, Phys. Rev. Lett. **130**, 207001 (2023).

[55] S. Das Sarma and H. Pan, Comment on "Trivial Andreev band mimicking topological bulk gap reopening in the nonlocal conductance of long Rashba nanowires," Phys. Rev. Lett. **132**, 099601 (2024).

[56] R. Hess, H. F. Legg, D. Loss, and J. Klinovaja, Hess Reply, Phys. Rev. Lett. **132**, 099602 (2024).

[57] D. A. Ivanov, Non-Abelian statistics of half-quantum vortices in *p*-wave superconductors, Phys. Rev. Lett. **86**, 268 (2001).

[58] J. Alicea, Y. Oreg, G. Refael, F. von Oppen, and M. P. A. Fisher, Non-Abelian statistics and topological quantum information processing in 1D wire networks, Nat. Phys. **7**, 412 (2011).

[59] B. van Heck, A. R. Akhmerov, F. Hassler, M. Burrello, and C. W. J. Beenakker, Coulomb-assisted braiding of Majorana fermions in a Josephson junction array, New J. Phys. **14**, 035019 (2012).

[60] J. Liu, W. Chen, M. Gong, Y. Wu, and X. C. Xie, Minimal setup for non-Abelian braiding of Majorana zero modes, Sci. China: Phys., Mech. Astron. **64**, 117811 (2021).

[61] R. V. Mishmash, B. Bauer, F. von Oppen, and J. Alicea, Dephasing and leakage dynamics of noisy Majorana-based qubits: Topological versus Andreev, Phys. Rev. B **101**, 075404 (2020).

[62] I. C. Fulga, B. van Heck, M. Burrello, and T. Hyart, Effects of disorder on Coulomb-assisted braiding of Majorana zero modes, Phys. Rev. B **88**, 155435 (2013).

[63] J. Manousakis, C. Wille, A. Altland, R. Egger, K. Flensberg, and F. Hassler, Weak measurement protocols for Majorana bound state identification, Phys. Rev. Lett. **124**, 096801 (2020).

[64] E. Mascot, T. Hodge, D. Crawford, J. Bedow, D. K. Morr, and S. Rachel, Many-body Majorana braiding without an exponential Hilbert space, Phys. Rev. Lett. **131**, 176601 (2023).

[65] C. Peeters, T. Hodge, E. Mascot, and S. Rachel, Effect of impurities and disorder on the braiding dynamics of Majorana zero modes, Phys. Rev. B **110**, 214506 (2024).

[66] H. Pan and S. Das Sarma, Crossover between trivial zero modes in Majorana nanowires, Phys. Rev. B **104**, 054510 (2021).

[67] H. Pan and S. Das Sarma, Physical mechanisms for zero-bias conductance peaks in Majorana nanowires, Phys. Rev. Res. **2**, 013377 (2020).

[68] L. T. Xu, J. Bai, W. Feng, and X. Q. Li, Dynamics simulation of braiding two Majorana zero modes via a quantum dot, Phys. Rev. B **108**, 115411 (2023).

[69] W. Chen, J. Wang, Y. Wu, J. Qi, J. Liu, and X. C. Xie, Non-Abelian statistics of Majorana zero modes in the presence of an Andreev bound state, Phys. Rev. B **105**, 054507 (2022).

[70] J. Fu, Majorana orthogonal transformation and Majorana zero modes in free fermionic systems, Ann. Phys. (NY) **432**, 168564 (2021).

[71] J. Fu, Properties and application of SO(3) Majorana representation of spin: Equivalence with Jordan-Wigner transformation and exact $Z_2$ gauge theories for spin models, Phys. Rev. B **98**, 214432 (2018).

[72] L. Wang, M. Troyer, and X. Dai, Topological charge pumping in a one-dimensional optical lattice, Phys. Rev. Lett. **111**, 026802 (2013).